






Research Article

Numerical Simulation of Ground Effect on Circulation Control Airfoil

Quanbing Sun ^{1,2}, Zhiwei Shi ^{1,2}, Weilin Zhang ^{1,2}, Zhikun Sun ^{1,2}
and Yongliang Chen ^{1,2}

¹College of Aerospace Engineering, Nanjing University of Aeronautics and Astronautics, Nanjing, Jiangsu, China

²Key Laboratory of Unsteady Aerodynamics and Flow Control, Ministry of Industry and Information Technology, Nanjing University of Aeronautics and Astronautics, Nanjing, Jiangsu, China

Correspondence should be addressed to Zhiwei Shi; szwam@nuaa.edu.cn

Received 12 April 2022; Revised 1 July 2022; Accepted 26 July 2022; Published 23 August 2022

Academic Editor: Jiaying Zhang

Copyright © 2022 Quanbing Sun et al. This is an open access article distributed under the Creative Commons Attribution License, which permits unrestricted use, distribution, and reproduction in any medium, provided the original work is properly cited.

Circulation control (CC) is used extensively to control the attitude of rudderless aircraft experiencing ground effect in take-off and landing phases. The investigation of ground effect on airfoil CC is necessary to improve flight performance and quality in proximity to the ground. The aerodynamics and flow field of a modified NACA0012 airfoil with CC in ground effect are investigated with numerical simulations. The compressible Reynolds-averaged Navier–Stokes equations with the shear-stress transport $k-\omega$ turbulence model equations are solved using the Finite Volume Method (FVM). Simulation results show that the ground effect changes the lift increment per unit jet momentum coefficient, and CC can reverse the polarity ground effect. The effective angle of attack α_E and the downwash space downstream airfoil are altered by the ground effect resulting in variations of airfoil surface pressure and lift. Unlike the unbounded flow field, the jet attachment distance is not only determined by the jet momentum coefficient but it can change with the ride height, which is the distance from the ground to the center of the semicircular Coanda surface, for the same jet momentum coefficient.

1. Introduction

Active flow control (AFC) has the potential to fly aircraft without control surfaces [1, 2]. Using AFC could reduce vehicle weight and the complexity of the mechanical structure while maintaining the same flight performance. The absence of the edges and gaps, resulting from movement control surfaces, reduces the signatures of military aircraft [3], enhancing their survivability in increasingly sophisticated threat environments.

Circulation control (CC) is one of the most widely used AFC techniques in rudderless aircraft and is based on the Coanda effect, changing wing circulation and lift by blowing air tangentially along the rounded trailing edge. CC was first proposed by Davidson [4] in 1962, and several researchers further developed the flow mechanism. Englar [5–7] investigated high lift performance and proposed that the lift incre-

ment increased with jet moment coefficient as long as the jet remained attached to the Coanda trailing edge. It was also found that the slot height to Coanda surface radius ratio h_s/r and Coanda surface radius to chord length ratio r/c impacted the maximum lift increment $\Delta C_{L,max}$ generated by CC. Abramson and Rogers [8] found that a supersonic jet would separate from the Coanda trailing edge because of shock wave and boundary layer interaction, leading to severe lift reduction. Llopis-Pascual [9] and Forster and Steijl [10] suggested that introducing a step between the jet exit and the Coanda surface can delay the separation of the supersonic Coanda jet. Chu et al. [11] showed that the elliptical Coanda trailing edge has better control consistency at different free-stream Mach numbers and better control stability with a supersonic jet.

Many applications of CC have been achieved. As early as the 1970s, circulation control technology was applied to

aircraft. The US Navy used CC to enhance the lift of the A-6A in take-off and landing processes [12, 13]. In 1976, the University of Virginia used CC to improve lift and the performance improvement is equivalent to a 20% increase in chord length [12, 13]. The Tutor UAV without ailerons using CC as a rolling controller completed flight experiments in 2005 [3]. Wind tunnel experiments showed that the control moment produced by CC is sufficient to meet a rudderless fly-wing aircraft's trim and maneuvering requirements [14]. The DEMON UAV [15–19], using CC as the rolling and pitching controller, achieved flight without control surfaces in 2008. A V-tail aircraft [20] flew with a CC rolling controller in 2014, and a rudderless canard layout UAV [21] completed flight tests in 2015.

When an aircraft flies near the ground, the surrounding airflow is compelled to be parallel to the ground, and the flow field changes cause aerodynamics variations, which is ground effect. All aircraft experience and are greatly affected by ground effect during take-off and landing, and rudderless aircraft are no exception. Studying ground effect to increase the stability and safety of aircraft during take-off and landing is essential.

The aerodynamics and flow physics of two-dimensional (2D) airfoils in ground effect have been broadly investigated. The exploration of the effect of camber and thickness on the aerodynamics of a 2D airfoil in ground effect was conducted by Hsiun and Chen [22] using numerical simulation. It was found that the channel between the lower airfoil surface and the ground determined the aerodynamics of the airfoil. Ahmed et al. [23] experimentally investigated ground effect on a NACA4412 airfoil, and it was indicated that the drag increased with the decrease of the ride height. However, the lift variations depended on the passage's shape between the lower airfoil surface and the ground. Zerihan and Zhang [24] and Mahon and Zhang [25] studied ground effect on a Tyrrell-02 airfoil with numerical simulations and wind tunnel experiments, and it was found that the reduction in ride height caused an initial increase of downforce, followed by a significant decrease as the ride height decreased. Qu et al. [26] performed numerical simulations to investigate ground effect on a NACA4412 airfoil for a wide angle of attack range and showed that the flow physics changed with the angle of attack. Nirooei [27] investigated the aerodynamic and static stability characteristics of airfoils in extreme ground effect using a computational method. However, there are few studies on ground effect for airfoils with CC. It is necessary to study aerodynamics and flow physics of the ground effect on an airfoil with CC to improve the performance of rudderless aircraft.

This paper investigates the aerodynamics and flow physics of a modified NACA0012 airfoil with CC in ground effect using Computational Fluid Dynamics (CFD). This paper is organized as follows. Section 1 introduces the present research achievement of the circulation control and the ground effect and puts forward the study focus of this paper. Section 2 gives the computational configuration and the validation of the numerical method. Section 3 shows the numerical result and analyses the flow physics of the ground effect on CC and Section 4 is the conclusion.

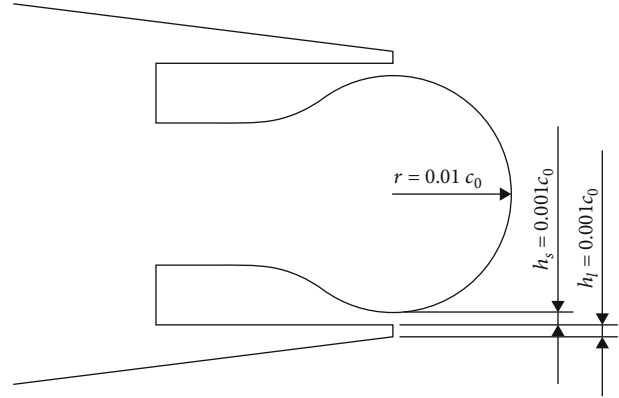


FIGURE 1: Coanda trailing edge of the modified airfoil.

2. Computational Configuration and Grid Resolution

2.1. Physical Model. The trailing edge of the baseline NACA0012 airfoil is truncated and replaced by a semicircular Coanda surface, and the chord length c of the modified airfoil is $0.93c_0$, where c_0 is the chord length of the baseline airfoil. Figure 1 shows the Coanda trailing edge of the modified airfoil. The radius of the Coanda surface is $0.01c_0$, and the slot height to radius ratio h_s/l is set to be 0.1 in this investigation. In addition, the height of the lip h_l between the lower surface of the airfoil and the slot is $0.001c_0$.

2.2. Numerical Method. The flow field for the airfoil is computed using the FLUENT CFD software. The compressible Reynolds-averaged Navier–Stokes (RANS) equations are solved with the shear-stress transport (SST) $k - \omega$ turbulence model using the finite-volume spatial discretization method. A second-order upwind scheme is used for calculating the convection terms, and a central difference scheme is used for the diffusion terms. The flux is discretized using Roe's approximate Riemann solver.

The rectangular computational domain used in the investigation is shown in Figure 2. The top, left, and right boundaries are located $20c_0$ away from the airfoil. The airfoil and jet plenum are set as no-slip static walls, and the jet source is set as the pressure inlet. The top, left, and right boundaries are set as pressure far field and the bottom boundary is a no-slip moving wall with a translational velocity equal to the free-stream velocity. The distance from the ground (the bottom boundary) to the center of the semicircular Coanda surface is defined as the ride height h , and its non-dimensional form is denoted as h/c .

The Reynolds number based on the chord length is 4.3×10^6 with free-stream Mach number $M = 0.2$. The non-dimensional ride heights $h/c = \text{inf}, 1.0, 0.8, 0.6, 0.4, 0.2$ with $\alpha = 0, 4, \text{ and } 8^\circ$ are considered in this investigation. For the $h/c = \text{inf}$ cases, the bottom boundary is located $20c_0$ away from the airfoil and is set as pressure far field.

2.3. Jet Momentum Coefficient. The jet momentum coefficient is an important parameter measuring the jet strength

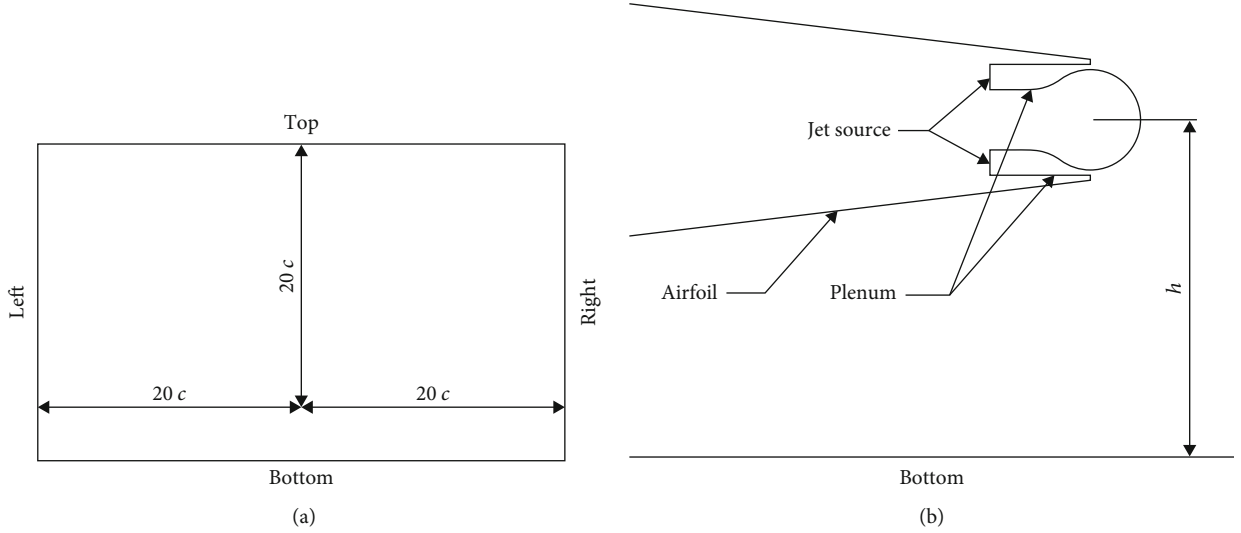


FIGURE 2: Rectangular computational domain and airfoil boundary: (a) rectangular computational domain; (b) airfoil boundary.

in circulation control. The 2D jet momentum coefficient is defined as:

$$C_{\mu} = \frac{\dot{m}U_{jet}}{q_{\infty}c}, \quad (1)$$

where c is reference chord length. The mass flow rate \dot{m} and jet velocity U_{jet} are determined by the nozzle pressure ratio NPR , defined as the ratio of the total plenum pressure P_0 to the free-stream static pressure P_{∞} , and the total temperature T_0 . The total temperature is fixed at 300K, and the jet momentum coefficient changes with the preset pressure ratio in the numerical simulation.

Because of the air viscosity, the jet is not isentropic, leading to non-uniform fluid density and jet velocity profiles at the nozzle outlet. Equation (1) can be rewritten in summation form to obtain a more accurate jet momentum coefficient:

$$C_{\mu} = \sum_{i=1}^N \frac{\rho_i v_i^2 \Delta h_i}{q_{\infty}c}, \quad (2)$$

where Δh_i is the spacing between neighboring grid points at the jet slot, and ρ_i and v_i are the fluid density and jet velocity of each cell on the interface boundary, respectively.

2.4. Validation of Numerical Method. First, a grid refinement study is conducted using the modified NACA0012 airfoil for upper slot blowing with $C_{\mu} = 0.013$ at $\alpha = 0^\circ$ and $h/c = 0.2$ and the free-stream Mach number is 0.2. The results are listed in Table 1. The Richardson extrapolation [28] method is used to estimate the coefficients on an “infinite” grid density. The formulation is defined as:

$$f_{inf} = f_2 + \frac{f_2 - f_1}{r^2 - 1}, \quad (3)$$

TABLE 1: Grid refinement study results.

Grid	Cell count	C_L	C_m
Coarse	1.16×10^5	0.6304	-0.1492
Medium	1.68×10^5	0.5202	-0.1342
Fine	2.44×10^5	0.5192	-0.1341
Extrapolation	Infinite	0.5171	-0.1338

where f_1 and f_2 are the simulation results of two sets of grids, and $r = 1.2$ is the grid refinement ratio of this investigation. As shown in Figure 3, C_L and C_m change significantly when the cell count increases from 1.16×10^5 to 1.68×10^5 . However, C_L and C_m change inconspicuously when the cell count increases from 1.68×10^5 to 2.44×10^5 . Richardson extrapolation results are listed in Table 1 and C_L and C_m produced by the medium grid are 0.6% greater and 0.34% less than the extrapolated results, respectively. It is concluded from these results that the medium grid gives acceptably accurate results while being computationally cost-effective.

Alexander et al. [29] conducted a range of experiments on a 0.75% cambered elliptical airfoil with a thickness of 6% chord to study the effects of CC. The span of the model was two chord lengths, and an end plate one chord length in diameter was installed. The aft 10% of the airfoil is truncated and installed with a 2.98 : 1 elliptical Coanda surface, and the slot height to chord ratio is 0.12%. The CC airfoil is illustrated in Figure 4.

Li and Qin [30] pointed out that the 2D airfoil case over-predicted the pressure coefficients on the surface, while the 3D model agreed well with the experimental data. Li and Qin [30] and Forster and Steijl [10] used an enlarged plate with a 1.1 chord length diameter to arrange the structured grid around the leading edge and improve the accuracy of the simulation. Thus, a 3D model with an enlarged plate is used in the simulation. The mesh domain of the model used in the investigation is shown in Figure 5 and Table 2 lists the

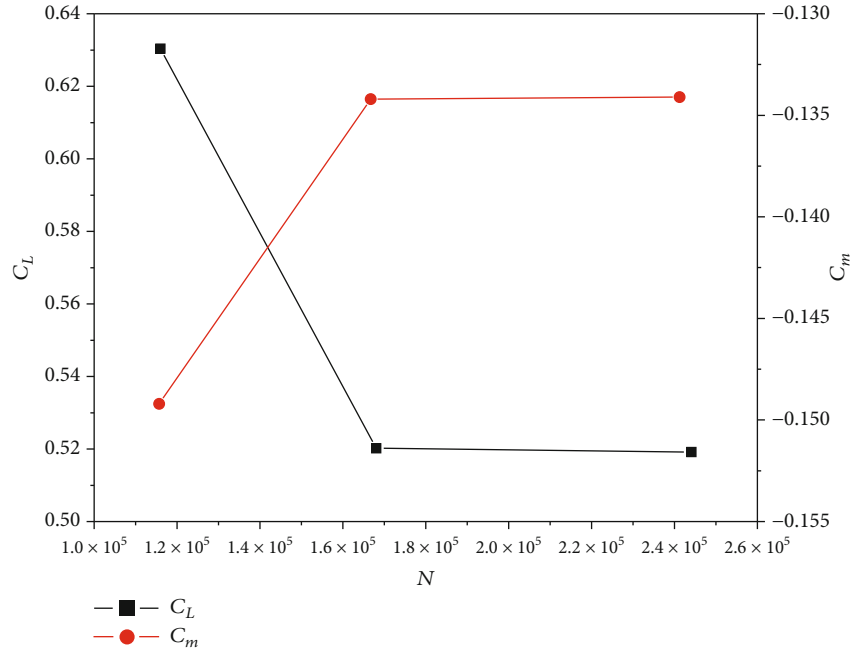


FIGURE 3: Curves of lift coefficient and pitch moment coefficient versus cell count.

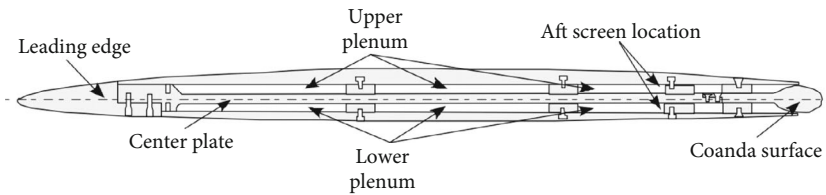


FIGURE 4: Elliptical airfoil with elliptical Coanda surface [29].

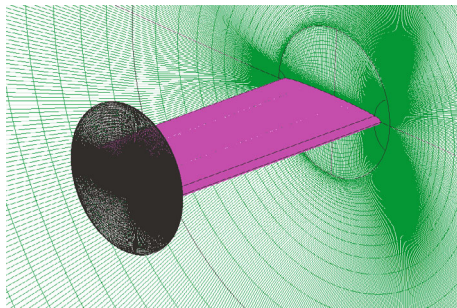


FIGURE 5: Mesh domain of the elliptical airfoil.

TABLE 2: 3D model and mesh information.

Name	Size
Chord length	30 inch
Span	60 inch
Cell counts	341 × 221 × 149 cells
Wall distance	$y^+ \leq 1$

size information of the model. The 3D mesh is generated with ICEM CFD and there are 221 cells on the main airfoil, 121 cells on the Coanda surface, 149 cells in the wall-normal direction, and 221 cells over the span of the airfoil. The distribution of grid points mentioned above is the same as that in Ref. [30] and the y^+ is less than 1.

A numerical simulation is conducted at $\alpha = 3^\circ$ with free-stream Mach number $M = 0.3$. Figure 6 compares the pressure coefficients from the numerical simulation and the experimental investigation at the model mid-span section, for upper slot blowing with jet momentum coefficient $C_{\mu} = 0.054$ and lower slot blowing with jet momentum coefficient $C_{\mu} = 0.028$. The computational pressure coefficients on the airfoil surface match the experimental data reasonably well, and the pressure distribution on the Coanda surface follows the trends of the experiment results.

There was a validation on the simulation of the ground effect of the airfoil using FLUENT [26] in the investigation of airfoil aerodynamics in ground effect for a wide angle of attack range. To further demonstrate that the aerodynamics of the airfoil with ground effect can be simulated with FLUENT, experimental data for a 2D NACA4412 airfoil with ground effect are used in the validation. As shown in

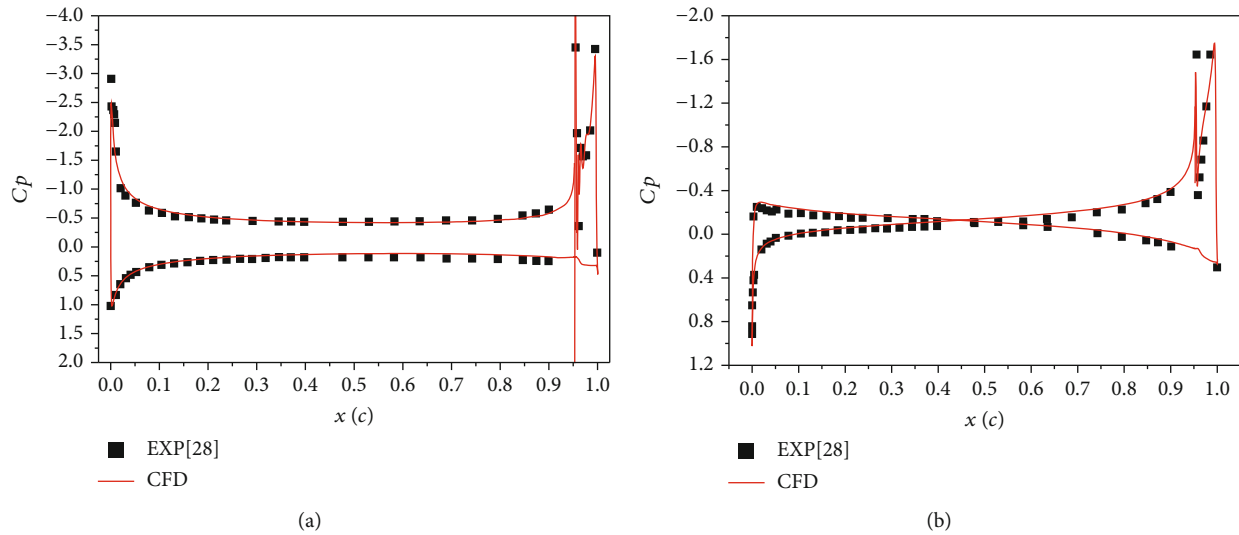


FIGURE 6: Comparison of pressure coefficient at the model mid-span section for CC validation: (a) upper slot blowing; (b) lower slot blowing.

Figure 7, the numerical pressure coefficient distribution agrees quite well with the experimental data from Ref. [23].

3. Results and Discussion

3.1. Lift Characteristics. Lift coefficient curves versus jet momentum coefficient at various ride heights are shown in Figure 8. A negative jet momentum coefficient indicates that the jet is ejected from the lower slot and a positive jet momentum coefficient indicates that the jet issues from the upper slot. It can be observed that the decrease of the ride height alters the slope of the lift coefficient curve, meaning that the ground effect has an impact on CC.

For the negative and a large range of the positive jet momentum coefficients, the lift decreases with reduced ride height at $\alpha = 0^\circ$ and decreases dramatically when the ride height h/c decreases to 0.2. For $\alpha = 0^\circ$, $|\Delta C_L|$ decreases with increasing jet momentum coefficient, where ΔC_L is defined as the difference between the lift of the unbounded flow field and the lift of the ground effect flow field with the same jet momentum coefficient. As the jet momentum coefficient increases further, negative ground effect evolves into positive ground effect, and the lift increases with reduced ride height for the airfoil with upper slot blowing at $C_\mu = 0.021$.

When the angle of attack increases to 4° , the lift increases with reduced ride height for the case without blowing and for upper slot blowing with $C_\mu < 0.021$. With increasing lower slot blowing $|C_\mu|$, positive ground effect evolves into negative ground effect for $h/c = 0.2$ and $h/c = 0.4$, showing that the ground effect polarity can be reversed by lower slot blowing.

The lift coefficient curves are almost parallel to each other for lower slot blowing at $\alpha = 8^\circ$, where ground effect has little influence on $\Delta C_L/\Delta C_\mu$. Positive ground effect appears for h/c ranging from 0.2 to 0.6 for upper slot blowing with $C_\mu < 0.014$. For $h/c = 0.8 \sim 1.0$, the lift changes

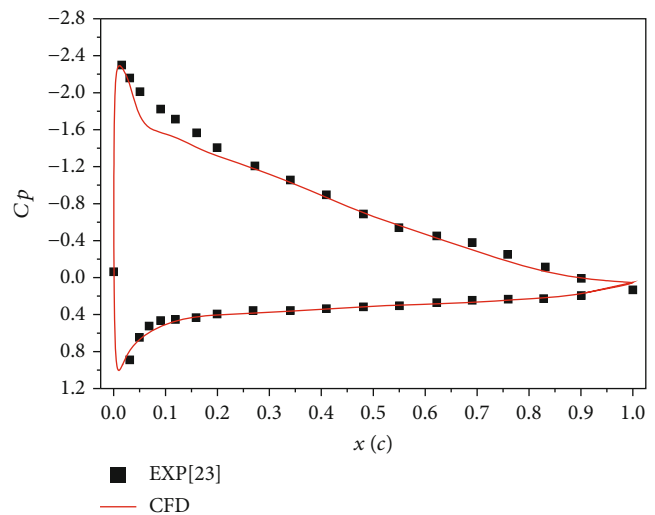


FIGURE 7: Comparison of pressure coefficient for ground effect validation.

modestly for cases without blowing and for upper slot blowing with $C_\mu < 0.014$.

It can be found in Figure 8 that the distribution of data points is complicated when $C_\mu > 0.018$ for $\alpha = 4^\circ$ and $C_\mu > 0.014$ for $\alpha = 8^\circ$. The preset NPR corresponding to the right-most points of each curve for $\alpha = 4^\circ$ are the same ($NPR = 1.25$), and the preset NPR corresponding to the two rightmost points of each curve for $\alpha = 8^\circ$ are 1.2 and 1.25, respectively. However, the jet momentum coefficient changes significantly with changing ride height, which is different from the other cases where the jet momentum varies little with decreasing h/c for the same preset NPR and α . As shown in Figure 9, C_μ decreases with reduced ride height instead of only depending on the preset NPR in these cases, where $h/c = 20$ represents the unbounded flow field.

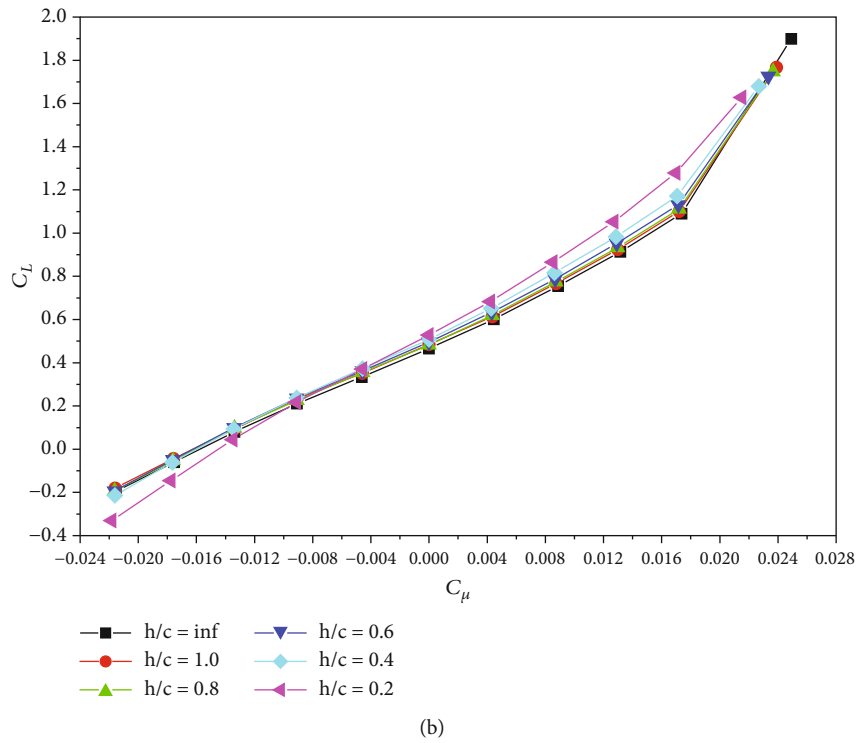
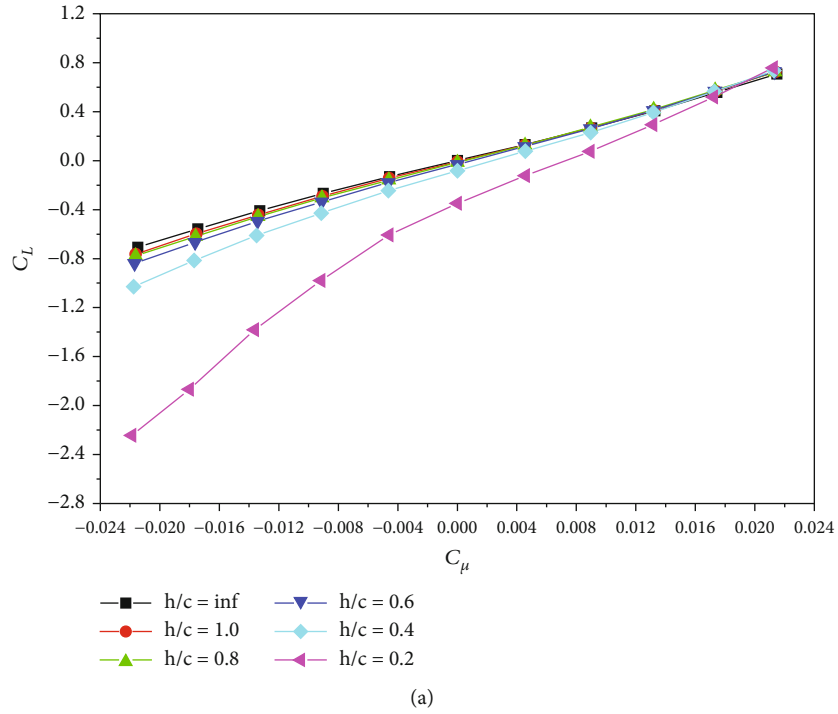


FIGURE 8: Continued.

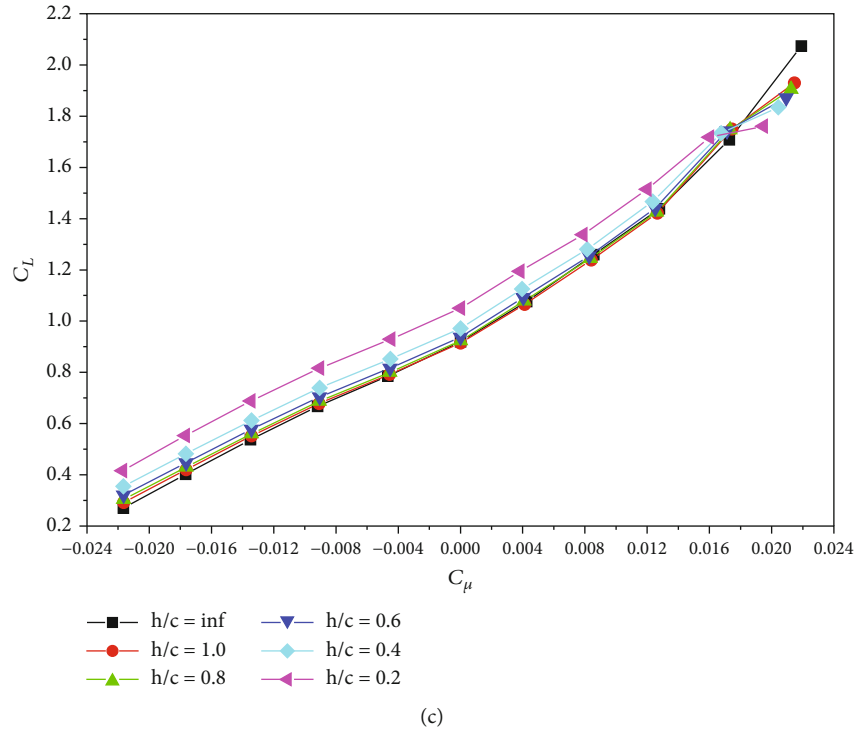


FIGURE 8: Curves of lift coefficient at various ride heights: (a) $\alpha = 0^\circ$; (b) $\alpha = 4^\circ$; (c) $\alpha = 8^\circ$.

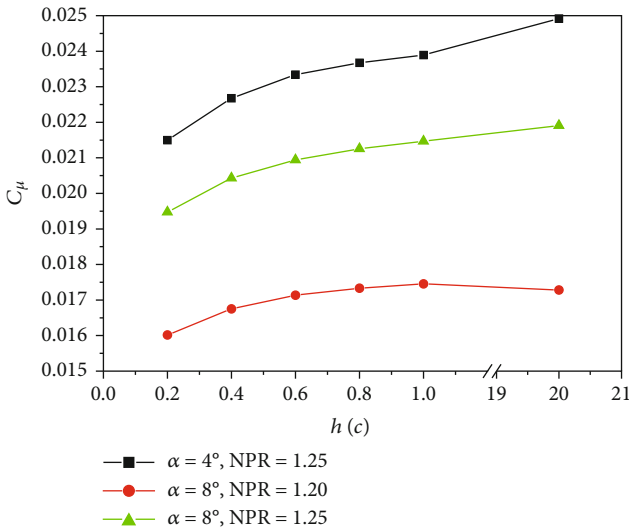


FIGURE 9: Curves of jet momentum coefficient versus ride height.

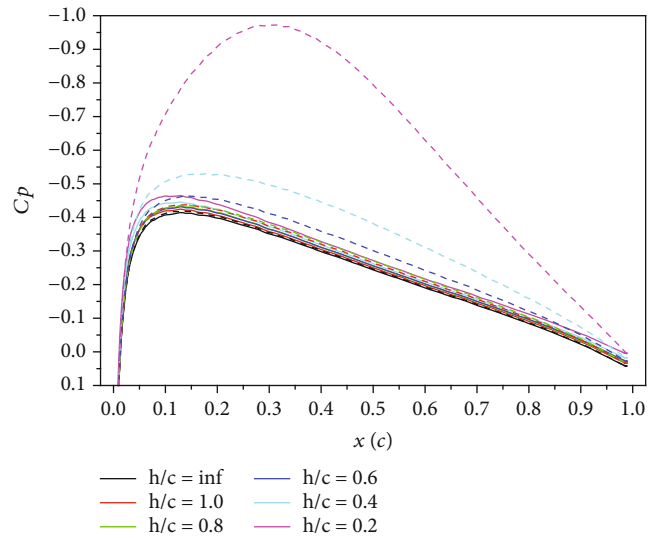


FIGURE 10: Pressure coefficient of the CC airfoil without blowing at $\alpha = 0^\circ$.

3.2. Results for $\alpha = 0^\circ$. Figure 10 shows the pressure coefficient distribution on the CC airfoil without blowing at various ride heights. The solid line represents the pressure distribution of the upper airfoil surface, and the dotted line with the same color is the pressure distribution on the lower airfoil surface for the same ride height. In the discussion to follow, $C_{p_{up}}$ and $C_{p_{low}}$ are the pressure coefficient of the main airfoil upper and lower surfaces, respectively, and $C_{L,up}$ and $C_{L,low}$ are the lift generated by the upper and lower

airfoil surfaces, respectively. When the ride height is reduced, $C_{p_{up}}$ decreases, resulting in the increasing $C_{L,up}$, while $C_{p_{low}}$ decreases first slowly and then quickly, resulting in the decreasing $C_{L,low}$; because $|\Delta C_{L,low}| > |\Delta C_{L,up}|$, ΔC_L is less than zero and decreases with the ride height. As shown in Figure 11, the flow channel between the lower airfoil surface and the ground is a convergent-divergent nozzle, and the flow accelerates to a maximum velocity at the throat and then

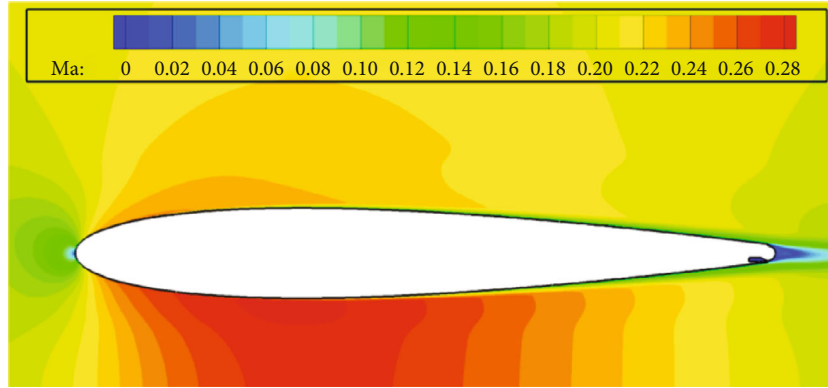


FIGURE 11: Mach number contours for airfoil without blowing at $h/c = 0.2$ and $\alpha = 0^\circ$.

decelerates. This is known as the Venturi effect, which creates a suction peak at the lower airfoil surface and an attractive lift reduction at h/c .

The two key streamlines are the leading and trailing edge stagnation streamlines [26] and are drawn with solid and dashed lines, respectively, in Figure 12 for cases without blowing at various ride heights. These two streamlines are nearly straight and located near $y/c = 0$ in the unbounded flow field. Although the stagnation streamlines are almost parallel to the ground in the far field, they deflect and become oblique lines as they approach the airfoil in the ground effect flow field. The section parallel to the ground gets closer to the ground with reduced ride height, and the deflection position approaches the airfoil, increasing the slope of the oblique section. As a result, the α_E close to the leading edge and the downwash space downstream of the trailing edge become larger with decreasing ride height so that the flow velocity and pressure of the upper airfoil surface increase and decrease, respectively.

In an unbounded flow field, the flows above the upper airfoil surface and below the lower airfoil surface are symmetrical about the airfoil chord. Thus, the pressure on either side of the streamline is virtually equivalent, and the stagnation streamline is level at around $y/c = 0$. The deflection of streamlines in the ground effect flow field can be explained by assuming that the streamlines stay at their original locations when the ground appears below the airfoil, as illustrated in Figure 13. As the flow accelerates in the narrower passage between the lower airfoil surface and the ground, there are a higher flow velocity and a lower pressure, propagating upstream and downstream. However, the original higher pressure is maintained on the upper side of the streamlines because there is no change in the upper flow field. Consequently, the two stagnation streamlines are extruded toward the passage and the ground under the action of the pressure difference. Finally, these streamlines stay in their new pressure equilibrium positions. A smaller ride height corresponds to a narrower passage formed by the lower airfoil surface and the ground. Thus, the pressure difference and offset of the streamline increase with reduced ride height.

The cases with $C_{\mu} = -0.014$ are selected for investigating the pressure distribution variation on the airfoil surface with

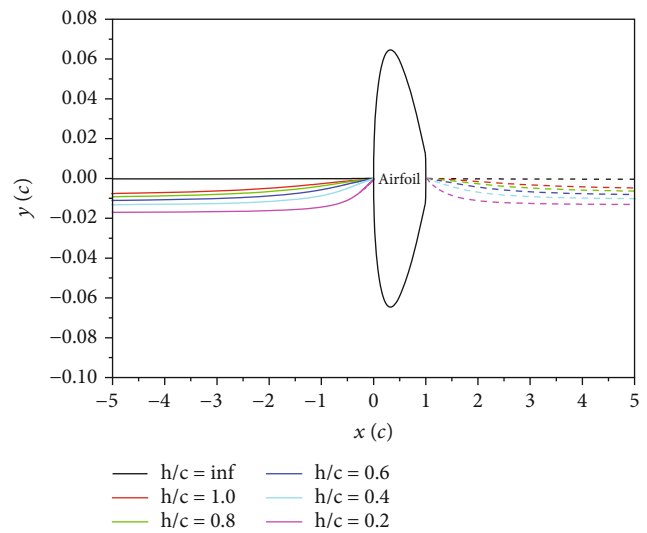


FIGURE 12: Leading and trailing edge stagnation streamlines for the no-blowing case at $\alpha = 0^\circ$.

decreasing ride height at $\alpha = 0^\circ$, as illustrated in Figure 14. For h/c ranging from infinity to 0.4, Cp_{up} decreases slightly with reduced height. For $h/c = 0.2$, Cp_{up} on the front section of the airfoil is almost the same as that for the $h/c = 0.4$ case, while it increases near $x/c = 0.85$ and becomes greater than that for the $h/c = \text{inf}$ case near $x/c = 0.95$. Cp_{low} decreases with decreasing ride height and shows an especially sharp reduction at $h/c = 0.2$ resulting from the Venturi effect.

For h/c ranging from infinite to 0.4, the pressure coefficient of the upper Coanda surface $Cp_{co,up}$ decreases slightly with reduced height. Yet for $h/c = 0.2$, $Cp_{co,up}$ is first greater than that for the $h/c = \text{inf}$ case and then decreases, forming a negative pressure zone near the trailing edge. The pressure coefficient of the lower Coanda surface $Cp_{co,low}$ decreases with reduced ride height, and there is a similarly sharp reduction in $Cp_{co,low}$ near the trailing edge for $h/c = 0.2$. Cp_{up} and $Cp_{co,up}$ change slightly with reduced ride height, resulting in little change in $C_{L,up}$. Remarkable decreases in Cp_{low} and $Cp_{co,low}$ lead to a large decrease in $C_{L,low}$ with

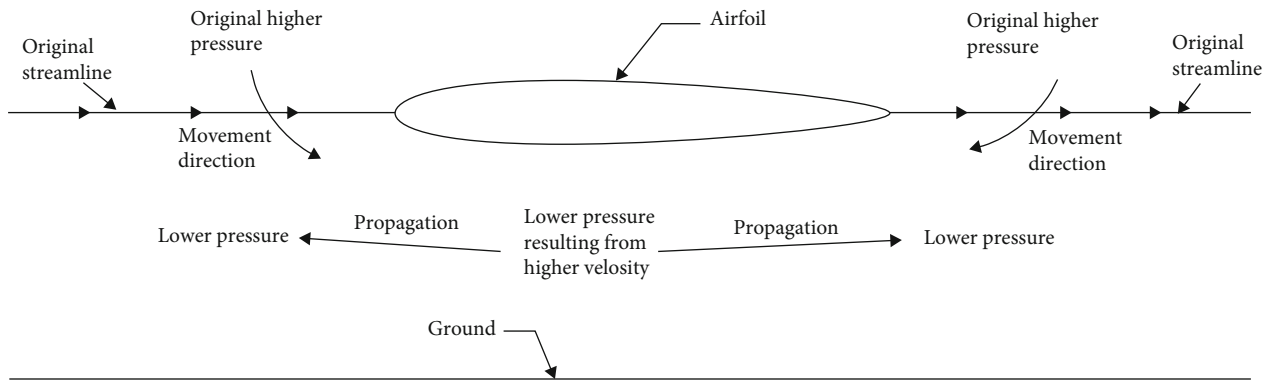


FIGURE 13: Principle of streamline deflection for the no-blowing case at $\alpha = 0^\circ$.

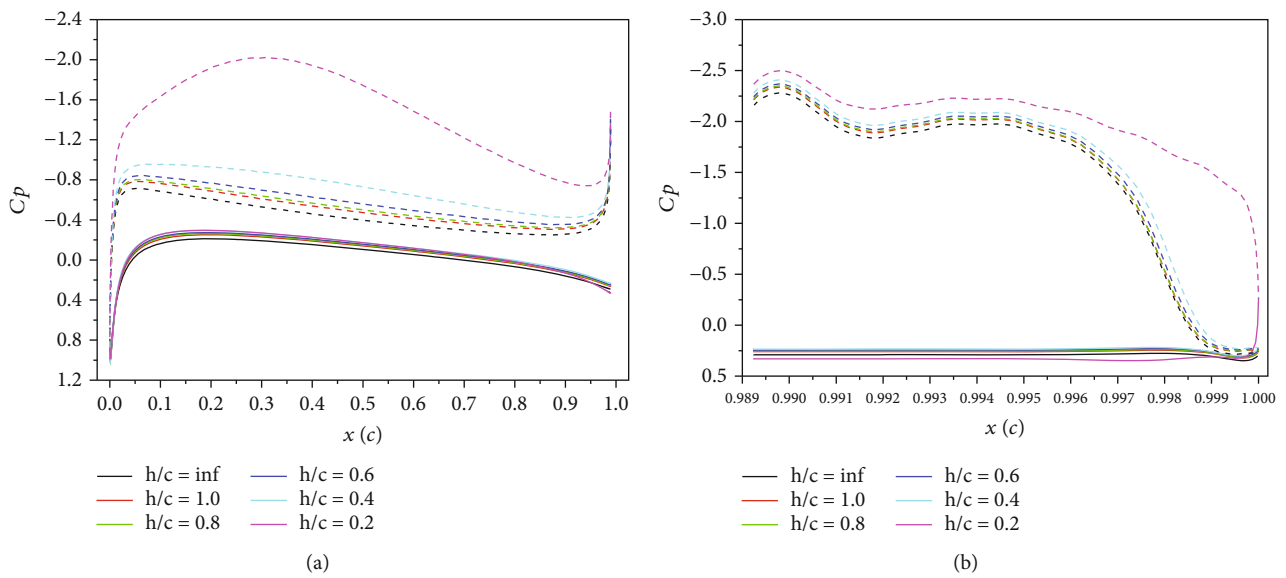


FIGURE 14: Pressure coefficient of the CC airfoil for blowing with $C_{\mu} = -0.014$ at $\alpha = 0^\circ$: (a) pressure coefficient of the main airfoil; (b) pressure coefficient of the Coanda surface.

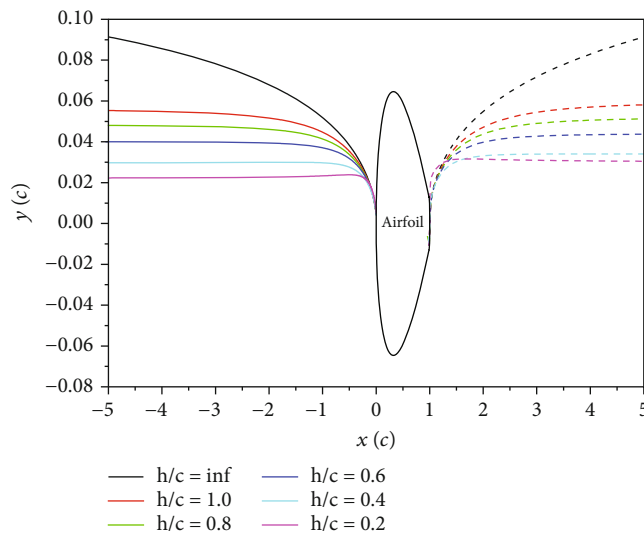


FIGURE 15: Leading edge stagnation streamlines and the streamlines beginning from the jet separation point on the Coanda surface for $C_{\mu} = -0.014$ at $\alpha = 0^\circ$.

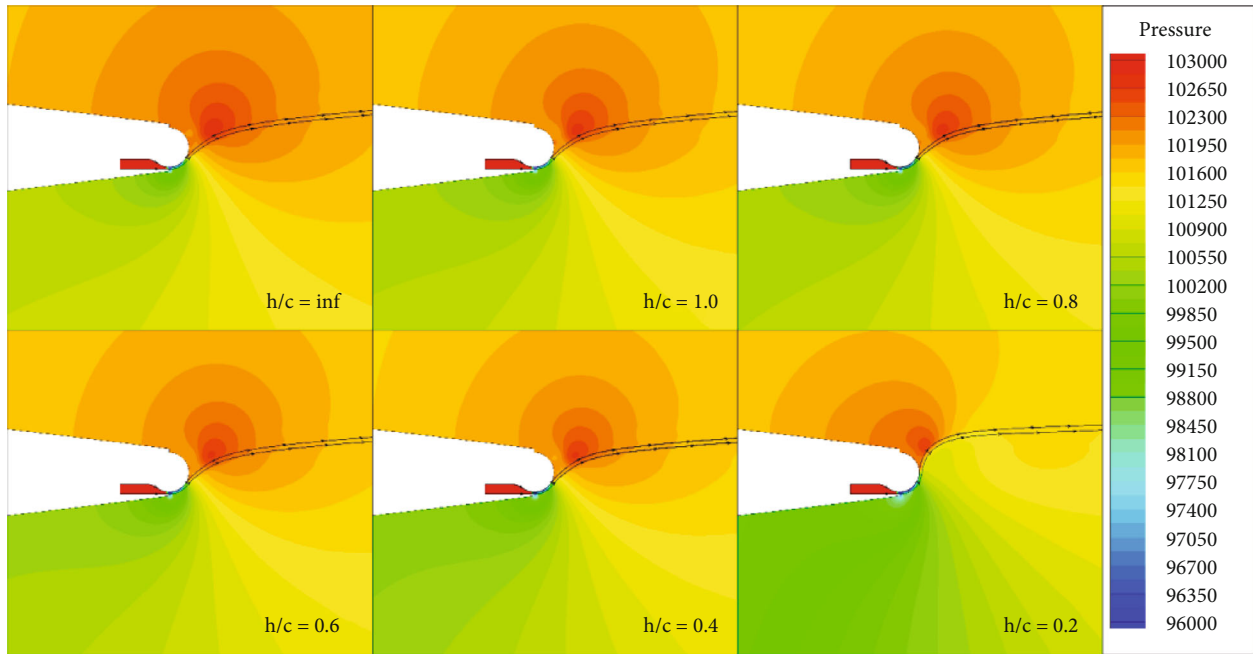


FIGURE 16: Pressure contours for $C_{\mu} = -0.014$ and $\alpha = 0^\circ$ at various ride heights.

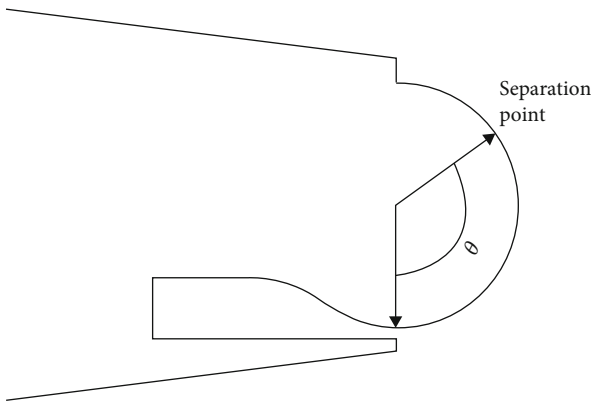


FIGURE 17: Definition of separation angle for the case with lower slot blowing.

reduced ride height, which is the main cause of the negative lift increment.

The two key streamlines for the blowing case are the streamline terminating at the airfoil leading edge stagnation and the streamline beginning from the jet separation point on the Coanda surface. These streamlines are shown in Figure 15 for various ride heights. The two streamlines deflect to approach and become parallel to the ground because of the pressure reduction below them with reduced ride height, similar to the no-blowing case. The deflection of the two streamlines relaxes the flow blockage up the airfoil, decreasing Cp_{up} with reduced ride height. Weakness of the upstream downwash and downstream upwash generally leads to a decrease of flow velocity below the airfoil and increase of Cp_{low} . However, the Venturi effect is stronger, resulting in decreasing Cp_{low} . Compared to the no-blowing

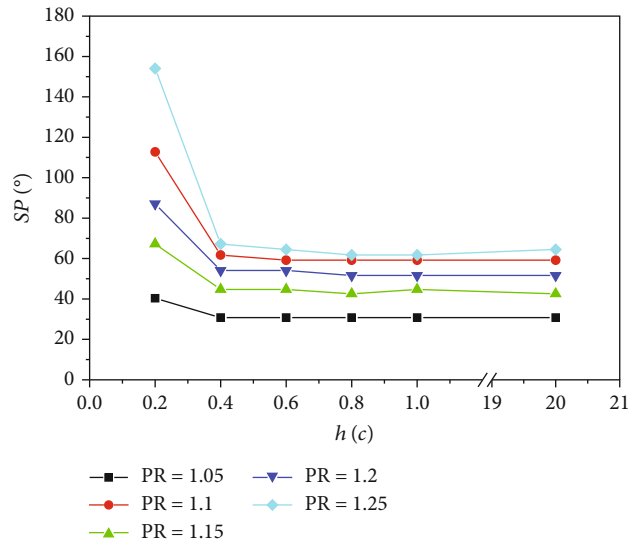


FIGURE 18: Curves of separation angle versus ride height for lower slot blowing with $\alpha = 0^\circ$.

case, a higher suction peak and lower Cp_{low} is formed on the lower airfoil surface for $h/c = 0.2$, because of a higher flow velocity resulting from the entrainment of the jet injected from the lower slot.

It can be observed that there is an obvious deformation of the jet streamline near the trailing edge for $h/c = 0.2$ in Figure 15. As shown in Figure 16, the higher pressure zone on the top right of the trailing edge narrows with the streamline deflection because of the relaxation of the local flow blockage. As the higher pressure zone continues to shrink, the jet gets closer to the upper airfoil surface when $h/c =$

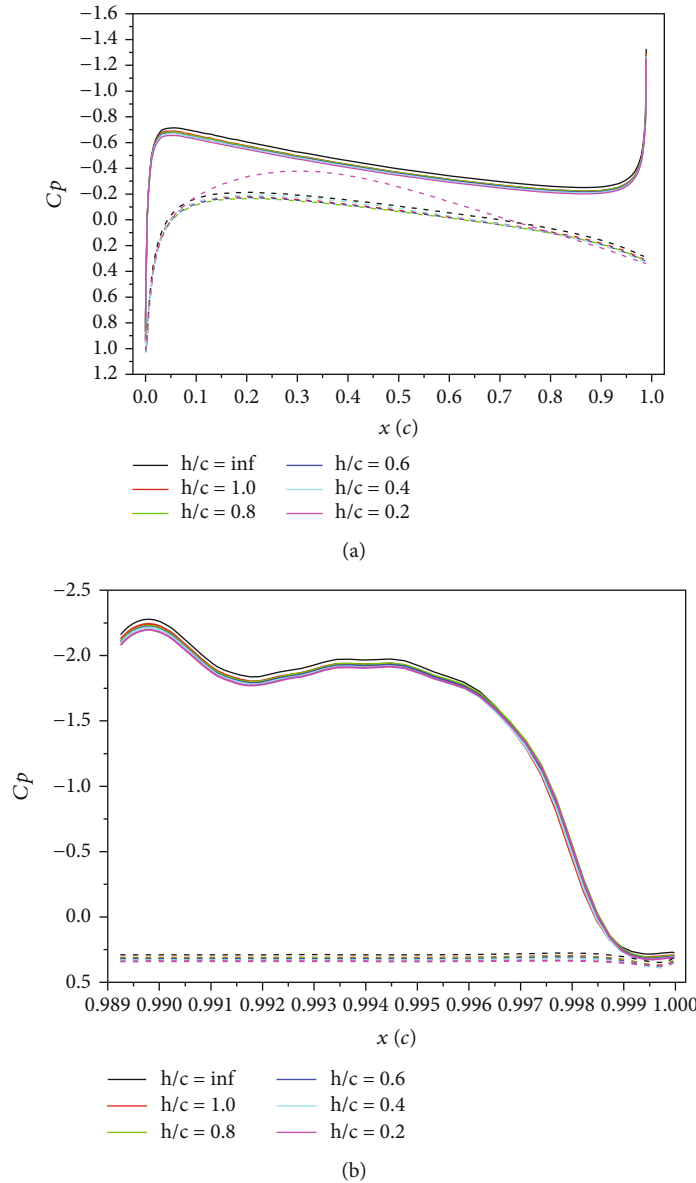


FIGURE 19: Pressure coefficient of the CC airfoil for blowing with $C_{\mu} = 0.014$ at $\alpha = 0^\circ$: (a) pressure coefficient of the main airfoil; (b) pressure coefficient of the Coanda surface.

0.2. It is considered that air gathers near the trailing edge and is squeezed toward the Coanda surface owing to the downward streamline deflection, forcing the jet to attach to the Coanda surface. Therefore, a small higher pressure zone approaches the upper airfoil surface, causing $C_{p_{up}}$ to increase near $x/c = 0.85$ and $C_{p_{co,up}}$ to become greater than that for the unbounded flow field at $h/c = 0.2$. The jet separation point then moves to the upper Coanda surface, resulting in a negative $C_{p_{co,up}}$ near the trailing edge.

Figure 16 shows that the jet attachment distance changes with ride height for the same jet momentum coefficient. In Figure 17, the jet attachment distance is compared using separation angle, defined as the central angle between the lower slot location and the jet separation location on the Coanda surface for the case with lower slot blowing. The

central angle of the whole Coanda surface is 180° for the present specific Coanda surface design.

Curves of separation angle versus ride height for various jet momentum coefficients are shown in Figure 18, with $h/c = 20$ representing the unbounded flow field. For the same ride height, the jet attachment distance increases with the jet momentum coefficient, which is consistent with previous studies. For h/c ranging from infinite to 0.4, the separation angle changes slightly with reduced ride height for the same jet momentum coefficient. Compared to the unbounded flow field, obvious increments of the jet attachment distance can be seen at $h/c = 0.2$ for various jet momentum coefficients.

Figure 19 shows the pressure coefficient distribution on the CC airfoil for blowing with $C_{\mu} = 0.014$ at various ride heights. The $C_{p_{up}}$ decreases with the ride height, and $C_{p_{low}}$

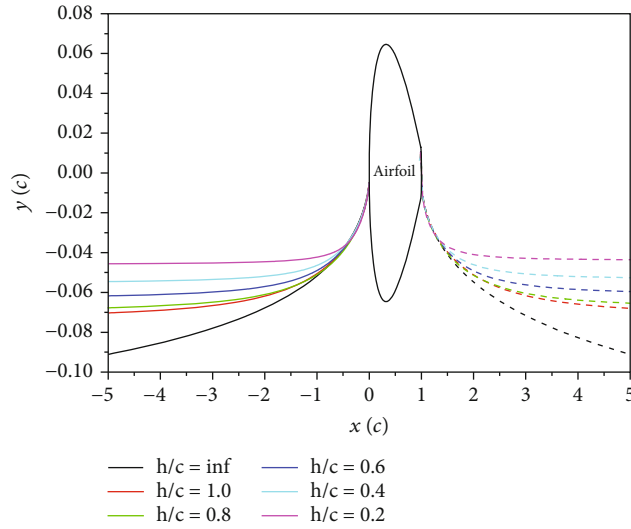


FIGURE 20: Leading edge stagnation streamlines and the streamlines beginning from the jet separation point on the Coanda surface for $C_{\mu} = 0.014$ at $\alpha = 0^\circ$.

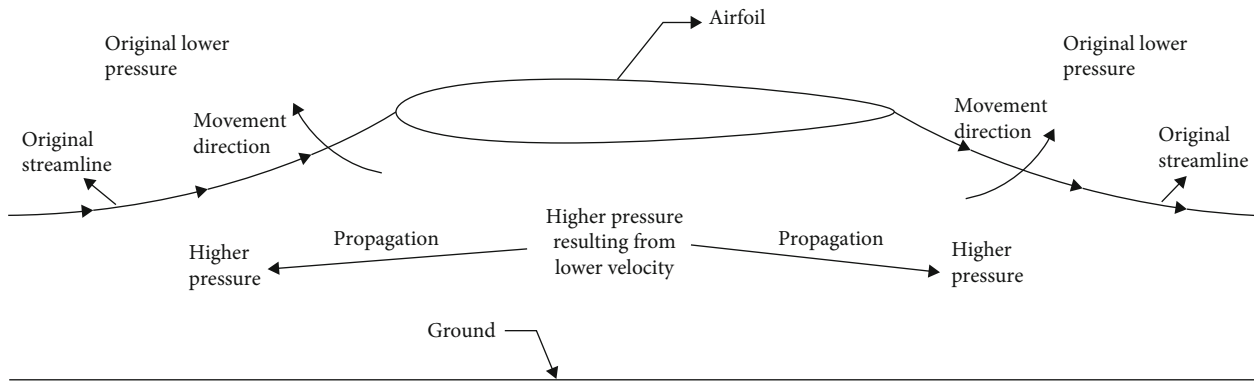


FIGURE 21: Principle of streamline deflection for upper slot blowing with $C_{\mu} = 0.014$ at $\alpha = 0^\circ$.

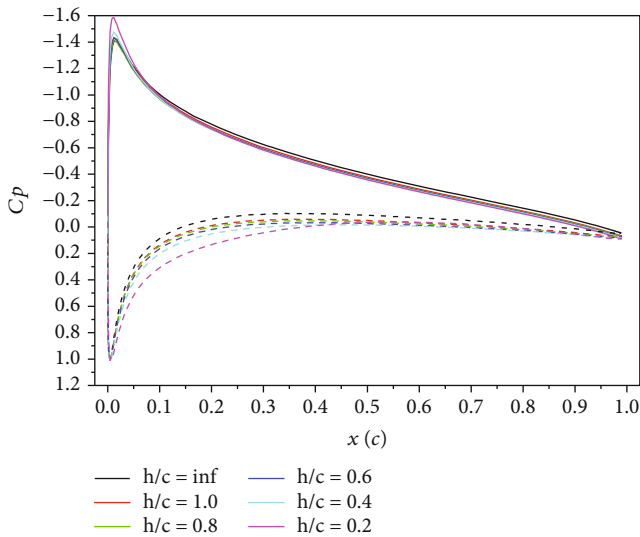


FIGURE 22: Pressure coefficient of the CC airfoil without blowing at $\alpha = 4^\circ$.

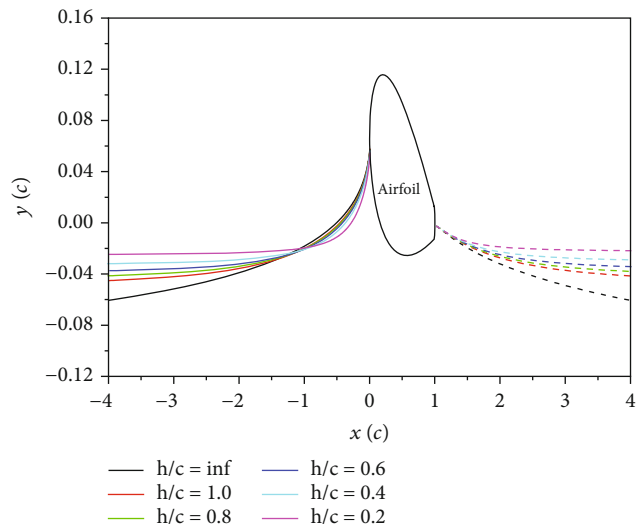


FIGURE 23: Leading and trailing edge stagnation streamlines for the no-blowing case at $\alpha = 4^\circ$.

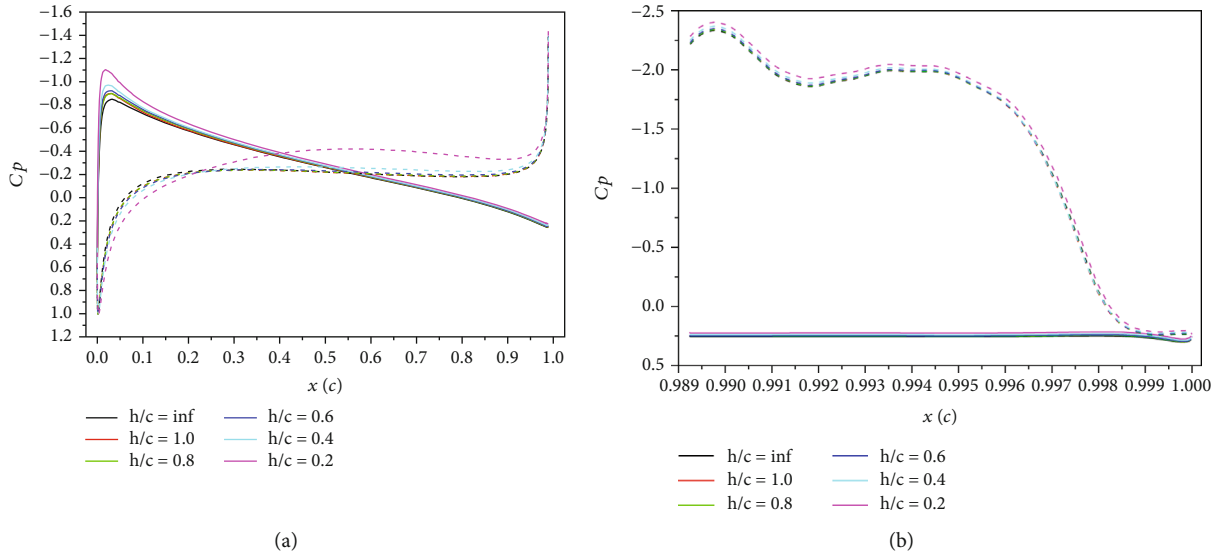


FIGURE 24: Pressure coefficient of the CC airfoil for blowing with $C_{\mu} = -0.013$ at $\alpha = 4^\circ$: (a) pressure coefficient of the main airfoil; (b) pressure coefficient of the Coanda surface.

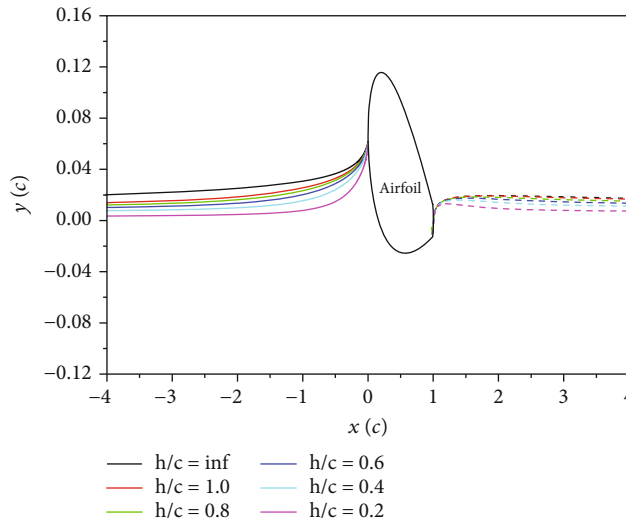


FIGURE 25: Leading edge stagnation streamlines and the streamlines beginning from the jet separation point on the Coanda surface for $C_{\mu} = -0.013$ at $\alpha = 4^\circ$.

increases for h/c ranging from infinite to 0.8 and decreases for h/c ranging from 0.8 to 0.4. When the ride height decreases to 0.2, $C_{p_{low}}$ is greater than the other cases in proximity to the leading edge, and there is a remarkable suction peak in the $C_{p_{low}}$ curve resulting from the Venturi effect. $C_{p_{co,up}}$ and $C_{p_{co,low}}$ change slightly with the reduced ride height. As a result, there is almost no change in lift for $h/c = 0.4 \sim \text{inf}$, while the airfoil with an intense Venturi effect is subjected to negative ground effect at $h/c = 0.2$.

The two sets of key streamlines at various ride heights are shown in Figure 20. The two streamlines deflect to approach and become parallel to the level line at $y/c = 0$. In contrast to the no-blowing cases, the upstream upwash and the downstream downwash space are reduced with decrease-

ing ride height so the flow velocity and pressure of the upper airfoil surface decrease and increase, respectively.

The pressure on either side of the streamline is balanced for the unbounded flow field, so streamlines stay at their original locations. As shown in Figure 21, the two streamlines, the lower airfoil surface, and the ground form a divergent-convergent channel when the airfoil approaches the ground. Thus, the flow decelerates and then accelerates in the channel resulting in higher pressure below the lower airfoil surface. Higher pressure propagates upstream and downstream and breaks the pressure balance, forcing the two streamlines to deflect upward. Hence, the two streamlines move to new positions forming a new pressure equilibrium.

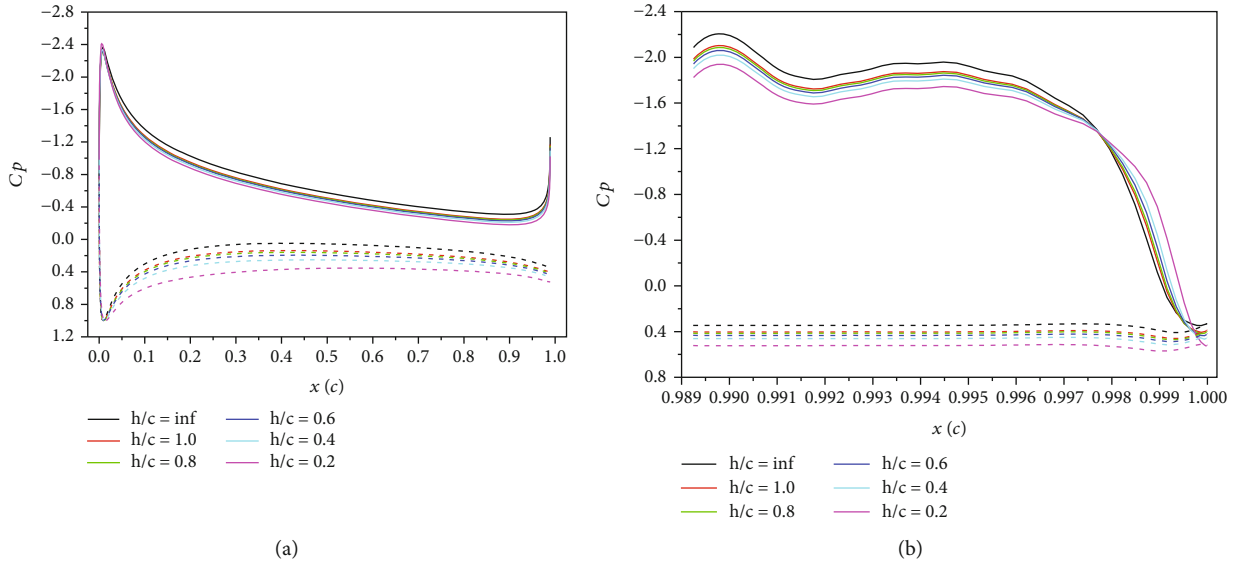


FIGURE 26: Pressure coefficient of the CC airfoil for blowing with $C_\mu = 0.013$ at $\alpha = 4^\circ$: (a) pressure coefficient of the main airfoil; (b) pressure coefficient of the Coanda surface.

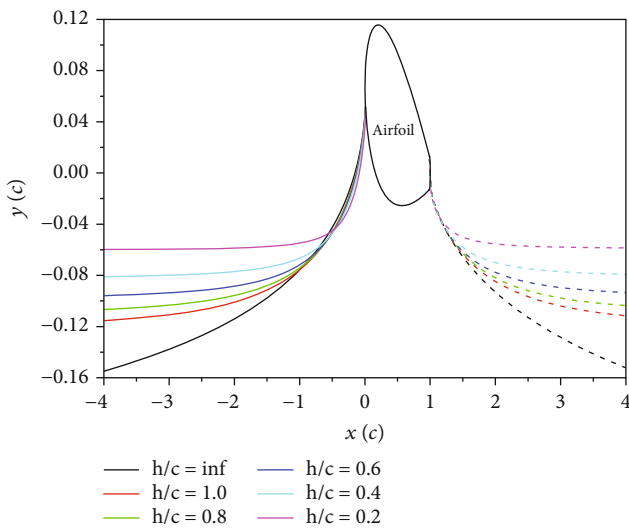


FIGURE 27: Leading edge stagnation streamlines and the streamlines beginning from the jet separation point on the Coanda surface for $C_\mu = 0.013$ at $\alpha = 4^\circ$.

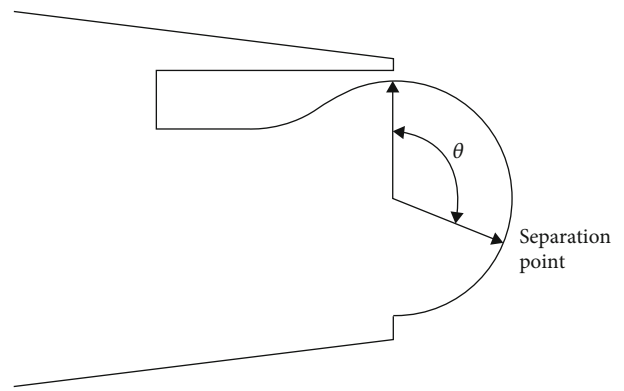


FIGURE 28: Definition of separation angle for upper slot blowing.

3.3. Results for $\alpha = 4^\circ$. Figure 22 shows the pressure coefficient distribution on the CC airfoil without blowing at various ride heights. $C_{p_{up}}$ increases slightly with reduced ride height and $C_{p_{low}}$ increases a little more quickly, resulting in a small positive ground effect. For $h/c = 0.2$ and $h/c = 0.4$, the upper airfoil surface suction peak is higher than that for the other cases. A moderate suction peak appears near $x/c = 0.55$ on the lower airfoil surface because the throat of the convergent-divergent passage moves backward with increasing α .

The two sets of key airfoil streamlines at various ride heights are shown in Figure 23. The main characteristics of streamline deflection are similar to the $\alpha = 0^\circ$, $C_\mu = 0.014$ cases, so the theory for the pressure coefficient variations is

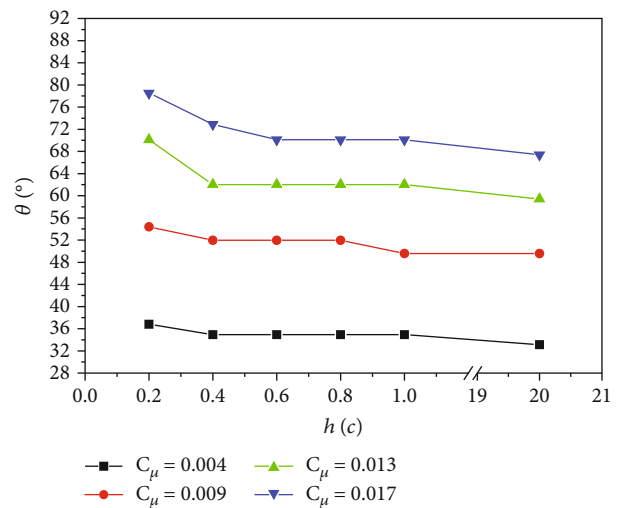


FIGURE 29: Curves of separation angle versus ride height for the airfoil with upper slot blowing at $\alpha = 4^\circ$.

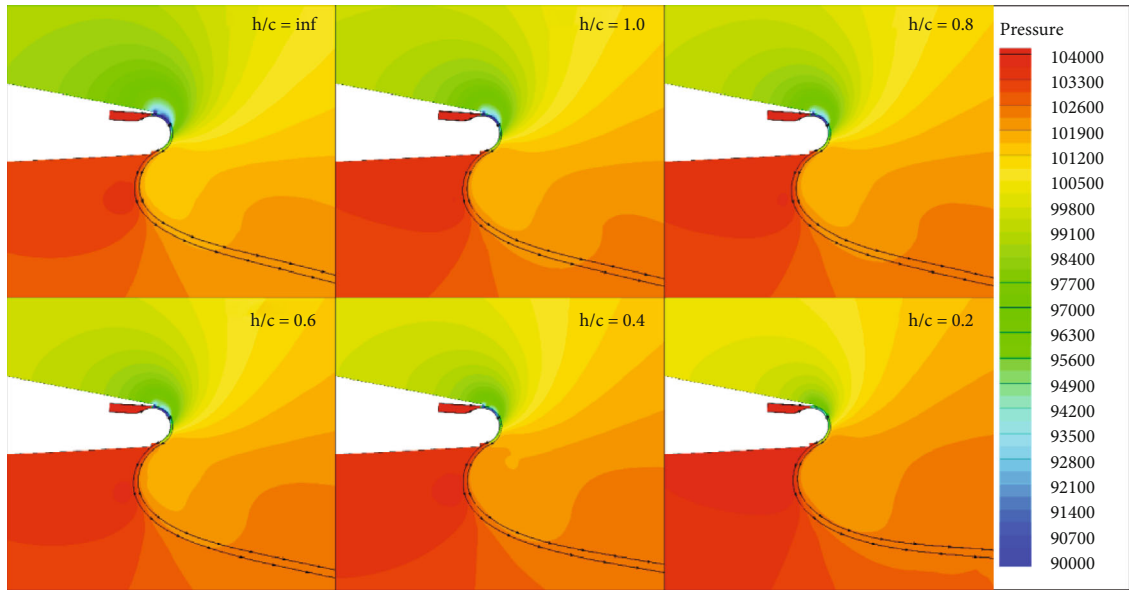


FIGURE 30: Pressure contours for $\alpha = 4^\circ$, $NPR = 1.25$ at various ride heights.

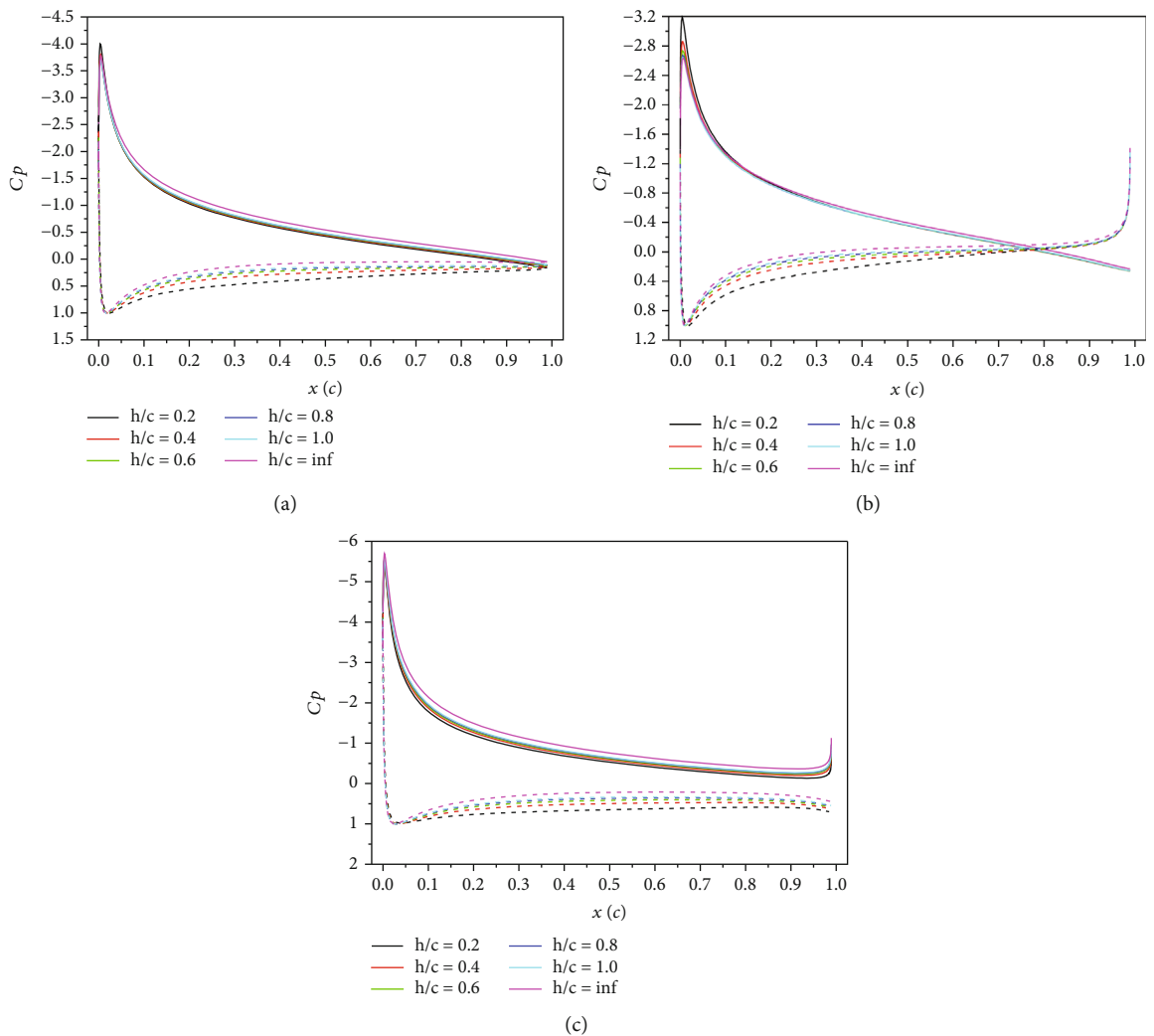


FIGURE 31: Pressure coefficients of the main airfoil at $\alpha = 8^\circ$: (a) without blowing; (b) with $C_{\mu} = -0.013$; (c) with $C_{\mu} = 0.013$.

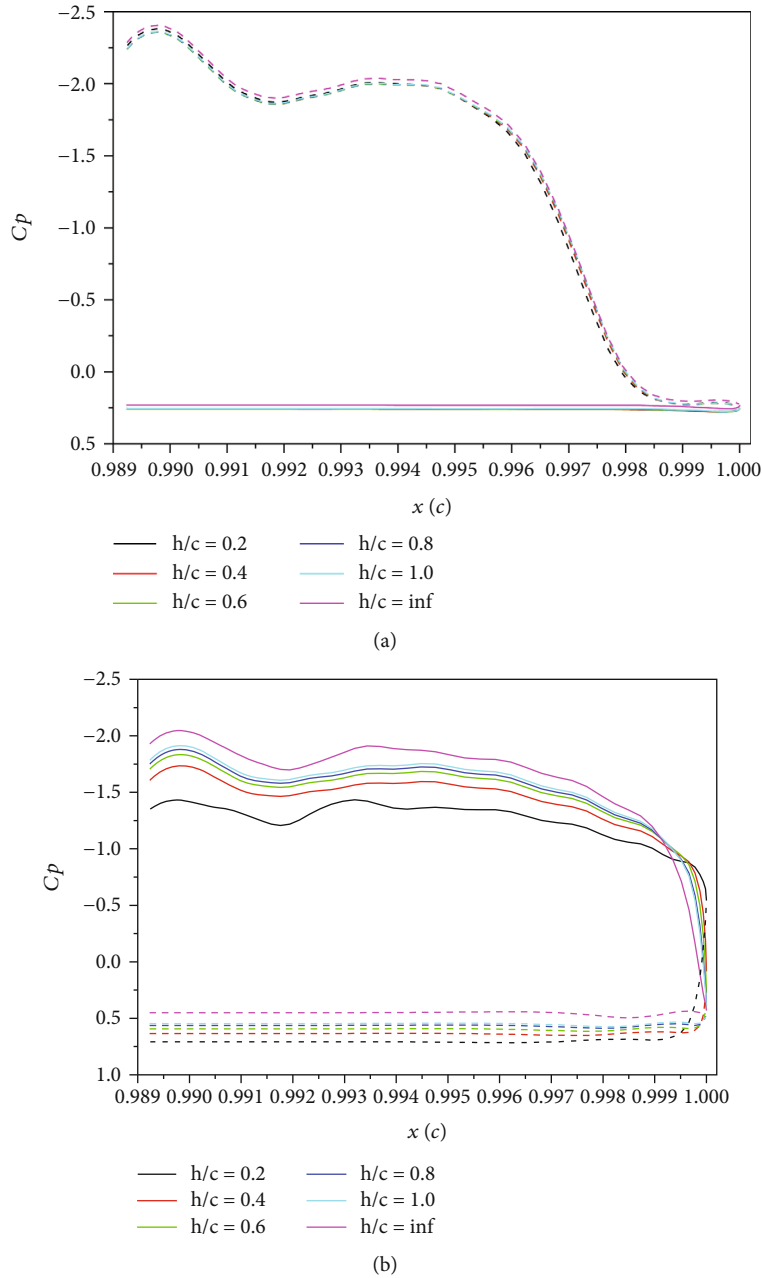


FIGURE 32: Pressure coefficients of the Coanda surface at $\alpha = 8^\circ$: (a) with $C_\mu = -0.013$; (b) with $C_\mu = 0.013$.

similar. A distinction is that the oblique section of the leading edge streamline is closer to the airfoil and the slope of the oblique section is higher for $h/c = 0.2$ and $h/c = 0.4$, which increases the α_E and the suction peak.

Figure 24 shows the pressure coefficient distribution on the CC airfoil for blowing with $C_\mu = -0.013$ at various ride heights. $C_{p_{up}}$ decreases slightly with reduced ride height and $C_{p_{low}}$ varies little except the $h/c = 0.2$ case. Thus, the lift changes slowly for $h/c = 0.4 \sim \text{inf}$. For $h/c = 0.2$, a higher pressure zone appears on the lower airfoil surface close to the leading edge, and a greater Venturi effect strengthens the lower airfoil surface suction. This enhanced Venturi effect is caused by flow acceleration due to jet

entrainment, resulting in negative ground effect. There is a little difference of $C_{p_{co,up}}$ and $C_{p_{co,low}}$ between various ride heights.

The streamline terminating at the airfoil leading edge stagnation point and the streamline beginning from the jet separation point on the Coanda surface at various ride heights are shown in Figure 25. The streamlines are drawn toward the ground and the passage between the lower airfoil surface and the ground because of the lower pressure in the passage, similar to the case without blowing at $\alpha = 0^\circ$. The slope of the oblique section, namely, the α_E , increases more obviously with reduced ride height, accounting for the higher suction peaks with smaller ride height.

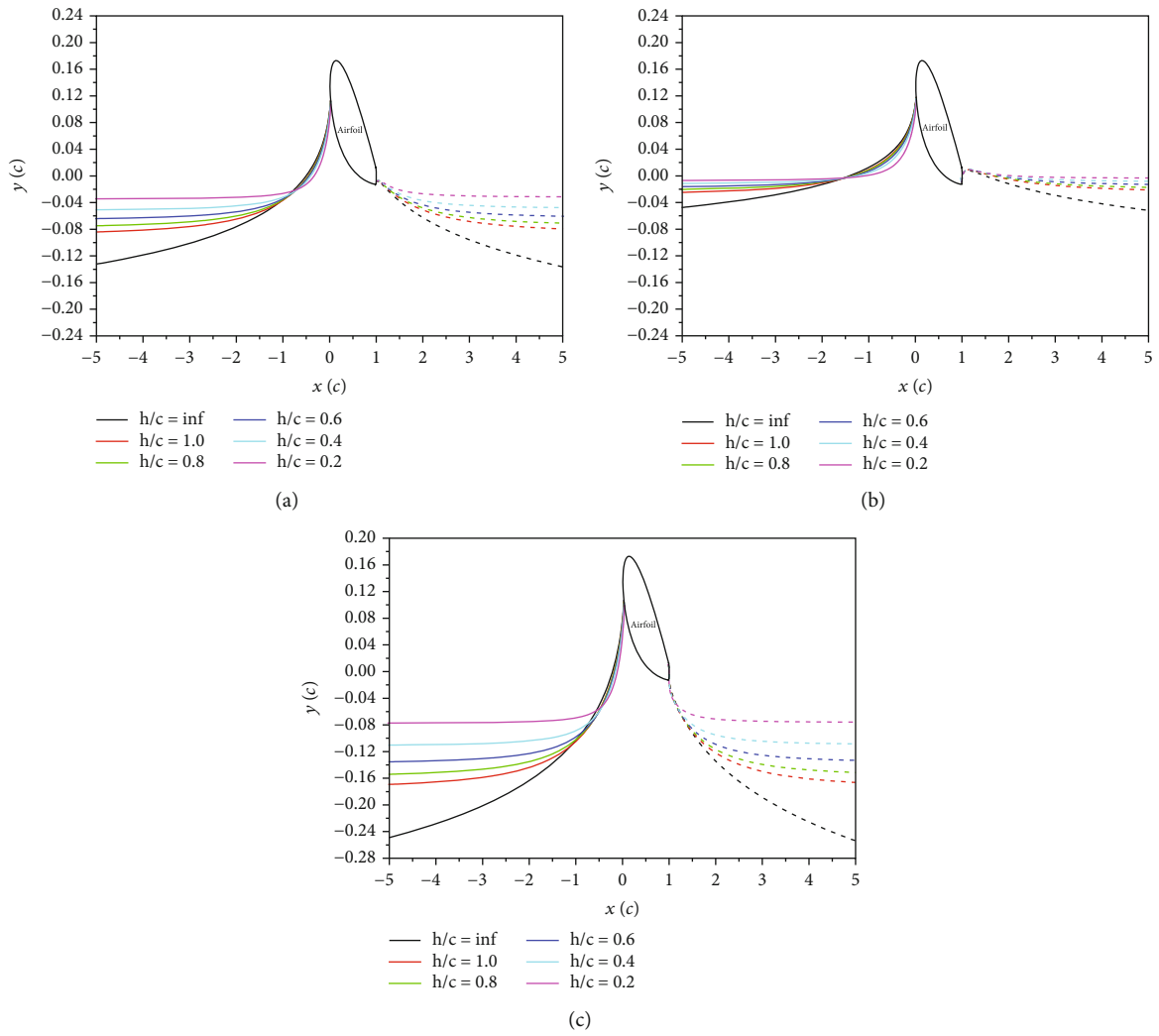


FIGURE 33: Two key streamlines for various ride heights at $\alpha = 8^\circ$: (a) without blowing; (b) with $C_\mu = -0.013$; (c) with $C_\mu = 0.013$.

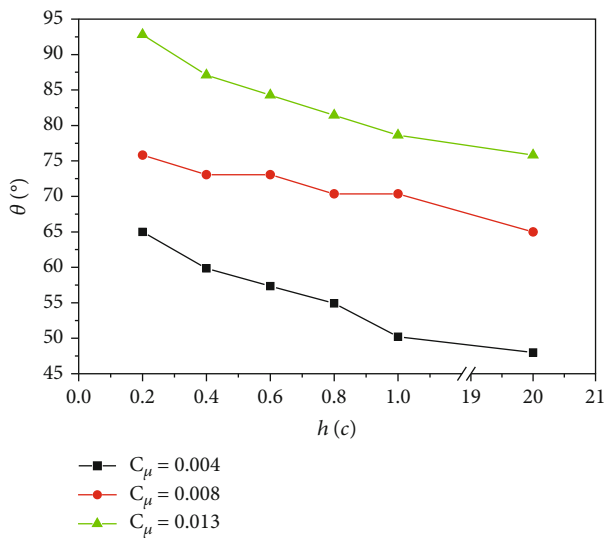


FIGURE 34: Curves of separation angle versus ride height for the airfoil with upper slot blowing and $C_\mu = 0.004 \sim 0.013$ at $\alpha = 8^\circ$.

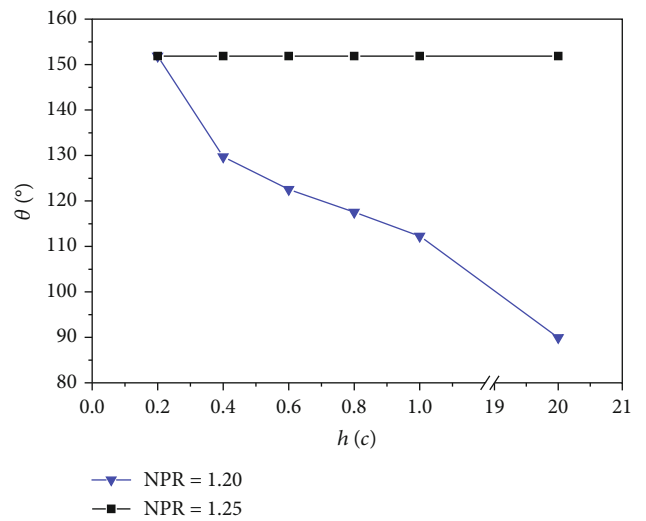


FIGURE 35: Curves of separation angle versus ride height for the airfoil with upper slot blowing and $NPR = 1.2 \sim 1.25$ at $\alpha = 8^\circ$.

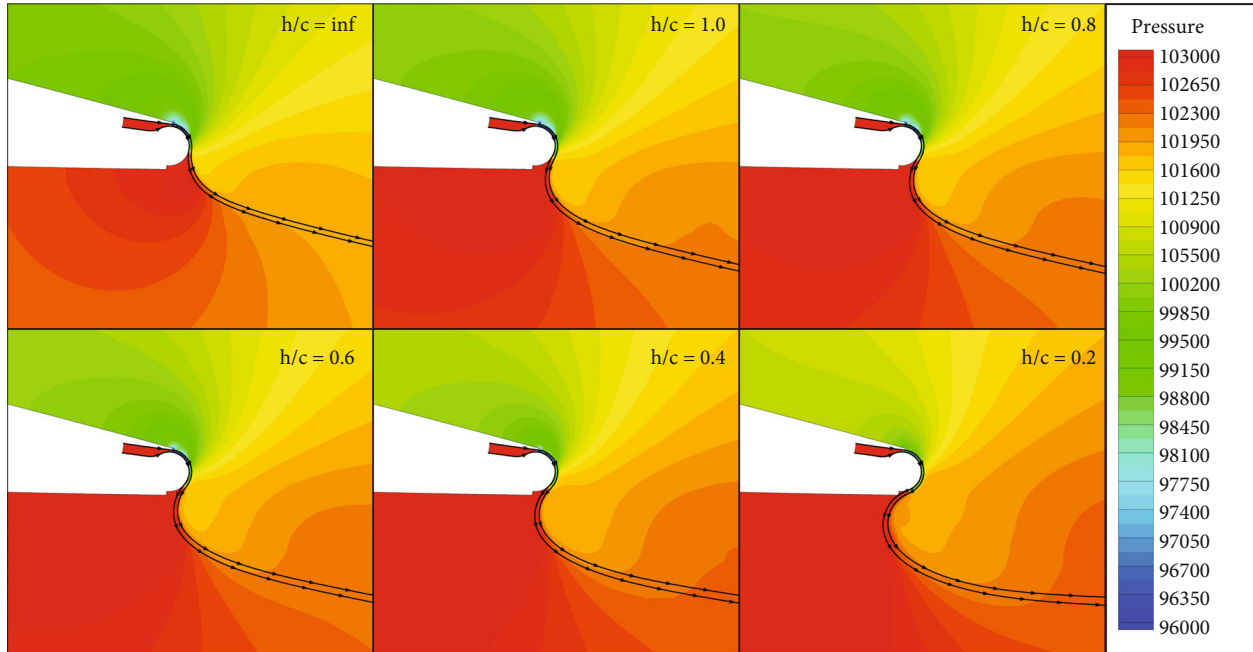


FIGURE 36: Pressure contours for $\alpha = 8^\circ$, $NPR = 1.2$ at various ride heights.

Figure 26 shows the pressure coefficient distribution on the CC airfoil for blowing with $C_{\mu} = 0.013$ at various ride heights. $C_{p_{up}}$, $C_{p_{low}}$, and $C_{p_{co,low}}$ increase when the ride height is reduced. $C_{p_{co,up}}$ decreases with ride height for x/c ranging from about 0.998 to 0.9995 and increases for the other x/c range. The increment of $C_{p_{low}}$ is slightly greater than that of $C_{p_{up}}$, resulting in positive ground effect. As shown in Figure 27, the deflection of the streamline is similar to the case with $C_{\mu} = 0.014$ at $\alpha = 0^\circ$.

For the case with upper slot blowing, the jet separation angle is defined as the central angle between the upper slot location and the jet separation location on the Coanda surface, as illustrated in Figure 28. As shown in Figure 29, the jet attachment distance increases with the reduced ride height for C_{μ} ranging from 0.004 to 0.017. When the preset NPR increases to 1.25, C_{μ} decreases with reduced ride height as mentioned above. And as shown in Figure 30, the CC evolves into the super-CC regime [31], and the separation point no longer varies with the change of the ride height. The maximum jet separation angle can only reach around 152° because there is a step between the lower wing and the Coanda surface. The attached jet travels over almost the entire Coanda surface, which can be seen as a jet flap. The effect of the jet flap on the lift enhancement is positively correlated with the jet momentum coefficient.

3.4. Results for $\alpha = 8^\circ$. Figure 31 shows the pressure coefficient distribution on the CC airfoil at various ride heights. $C_{p_{low}}$ increases with reduced ride height for the airfoil without blowing and the airfoil with blowing at $C_{\mu} = -0.013$ and $C_{\mu} = 0.013$. There is no suction peak on the lower airfoil sur-

face because the passage between the lower surface and the ground is only a convergent passage. $C_{p_{up}}$ increases for the airfoil without blowing and the airfoil with blowing at $C_{\mu} = 0.013$, and yet $C_{p_{up}}$ changes very little with changing ride height for blowing with $C_{\mu} = -0.013$.

As shown in Figure 32, the pressure on the upper and lower Coanda surfaces changes a little at various ride heights for the airfoil with blowing at $C_{\mu} = -0.013$. $C_{p_{co,up}}$ and $C_{p_{co,low}}$ increase with reduced ride height for the airfoil with blowing at $C_{\mu} = 0.013$.

The main characteristics of streamline deflections shown in Figure 33 are similar to the result for blowing with $C_{\mu} = 0.014$ at $\alpha = 0^\circ$. A more obvious slope increase can be observed with reduced ride height in the oblique section of the streamline for the airfoil with blowing at $C_{\mu} = -0.013$, which is responsible for the increase of the suction peak.

As shown in Figure 34, the jet attachment distance increases with reduced ride height for jet momentum coefficients ranging from 0.004 to 0.013. As mentioned above, when the preset NPR is increased to 1.2, C_{μ} decreases with ride height. However, as shown in Figure 35, the jet attachment distance increases when C_{μ} is reduced, which is different from the unbounded flow field cases in previous investigations. Air gathers near the trailing edge and is squeezed toward the Coanda surface because of the upward streamline deflection, forcing the jet to attach to the Coanda surface, as illustrated in Figure 36. A higher pressure zone grows with reduced ride height, indicating the air gathering and blocking near the trailing edge. The CC also evolves into the super-CC regime when the preset NPR increases to 1.25, so the jet separation angle remains near 152° .

4. Conclusion

The ground effect on the CC of a modified NACA0012 airfoil is investigated with numerical simulations using the FLUENT code. The variations of the lift coefficient and pressure distribution on the airfoil surface with changing ride height are illustrated and analyzed with the exhibition of the flow field. The following conclusions can be summarized from these investigations:

- (1) The slope of the lift coefficient curve versus jet momentum coefficient varies with decreasing ride height, meaning that ground effect alters the lift increment per unit jet momentum coefficient. The polarity of the ground effect can be reversed by CC
- (2) As the ground approaches, the original pressure balance on both sides of the stagnation streamline or the streamline beginning from the jet separation point on the Coanda surface is broken. Streamlines move under the action of pressure differences and then remain in the new pressure equilibrium position, which alters the flow field on either side of the streamlines resulting in changes of pressure distribution and lift coefficient
- (3) The jet attachment distance increased with reduced ride height for the airfoil with lower slot blowing at $\alpha = 0^\circ$ and the airfoil with upper slot blowing at $\alpha = 4^\circ$ and $\alpha = 8^\circ$ for the same jet momentum coefficient. For $\alpha = 8^\circ$, the jet momentum coefficient decreases with ride height when the preset NPR is 1.2, while the jet attachment distance increases, which is different from the cases with unbounded flow field

Data Availability

The data that support the findings of this study are available from the corresponding author upon reasonable request (szwam@nuaa.edu.cn).

Conflicts of Interest

The authors declare that they have no conflicts of interest or personal relationships that could have appeared to influence the work reported in this paper.

Acknowledgments

This work was partially supported by the National Natural Science Foundation of China (Grant No. 12072155) and Aeronautical Science Foundation of China (Grant No. 2019ZA052001).

References

- [1] D. R. Smith and C. Warsop, "NATO AVT-239 task group: innovative control effectors for manoeuvring of air vehicles-introduction and overview," in *AIAA Scitech 2019 Forum*, American Institute of Aeronautics and Astronautics, 2019.
- [2] C. Warsop, D. R. Smith, and D. Miller, "NATO AVT-239 task group: innovative control effectors for manoeuvring of air vehicles-conclusions and next steps," in *AIAA Scitech 2019 Forum*, American Institute of Aeronautics and Astronautics, 2019.
- [3] C. Warsop and W. J. Crowther, "Fluidic flow control effectors for flight control," *AIAA Journal*, vol. 56, no. 10, pp. 3808–3824, 2018.
- [4] I. M. Davidson, "Aerofoil boundary layer control systems," 1962, US Patent Office. Vol. US3062483 A, US.
- [5] R. J. Englar, *Two-Dimensional Transonic Wind Tunnel Tests of Three 15-Percent Thick Circulation Control Airfoils*, 1970.
- [6] R. J. Englar, "Experimental investigation of the high velocity Coanda wall jet applied to bluff trailing edge circulation control airfoils," *David W. Taylor Naval Ship Research and Development Center, Rept. Vol. 4708, Bethesda*, 1975.
- [7] R. J. Englar, R. A. Hemmerly, W. H. Moore, V. Seredinsky, W. Valckenaere, and J. A. Jackson, "Design of the circulation control wing STOL demonstrator aircraft," *Journal of Aircraft*, vol. 18, no. 1, pp. 51–58, 1981.
- [8] J. Abramson and E. Rogers, "High-speed characteristics of circulation control airfoils," in *21st Aerospace Sciences Meeting*, American Institute of Aeronautics and Astronautics, 1983.
- [9] A. Llopis-Pascual, *Supercritical Coanda Jets for Flight Control Effectors*, PhD diss., PhD Thesis, University of Manchester. (UNPUBLISHED WORK—awaiting resubmission), Manchester, 2017.
- [10] M. Forster and R. Steijl, "Numerical simulation of transonic circulation control," in *53rd AIAA Aerospace Sciences Meeting*, American Institute of Aeronautics and Astronautics, 2015.
- [11] Y. W. Chu, H. Y. Xu, C. L. Qiao, Y. H. Wang, and Y. Xu, "Computational evaluation of geometric effects on aerodynamic performance of circulation control airfoils," *Proceedings of the Institution of Mechanical Engineers, Part G: Journal of Aerospace Engineering*, vol. 235, no. 12, pp. 1717–1733, 2021.
- [12] J. L. Loth, "Advantages of combining BLC suction with circulation control high-lift generation," in *Applications of Circulation Control Technology*, pp. 3–22, American Institute of Aeronautics and Astronautics, Reston, VA, 2006.
- [13] R. J. Englar, "Overview of circulation control pneumatic aerodynamics: blown force and moment augmentation and modification as applied primarily to fixed-wing aircraft," in *Applications of Circulation Control Technology*, pp. 23–68, American Institute of Aeronautics and Astronautics, Reston, VA, 2006.
- [14] P. I. A. Wilde, W. J. Crowther, and C. D. Harley, "Application of circulation control for three-axis control of a tailless flight vehicle," *Proceedings of the Institution of Mechanical Engineers, Part G: Journal of Aerospace Engineering*, vol. 224, no. 4, pp. 373–386, 2010.
- [15] P. Wilde, K. Gill, S. Michie, and W. Crowther, "Integrated design of fluidic flight controls for a flapless aircraft," in *46th AIAA Aerospace Sciences Meeting and Exhibit*, American Institute of Aeronautics and Astronautics, 2008.
- [16] P. Wilde, A. Buonanno, W. Crowther, and A. Savvaris, "Aircraft control using fluidic maneuver effectors," in *26th AIAA Applied Aerodynamics Conference*, Honolulu Hawaii, 2008.
- [17] J. P. Fielding, A. Mills, and H. Smith, "Design and manufacture of the DEMON unmanned air vehicle demonstrator vehicle," *Proceedings of the Institution of Mechanical Engineers, Part G: Journal of Aerospace Engineering*, vol. 224, no. 4, pp. 365–372, 2010.

- [18] J. Fielding, C. Lawson, R. Martins-Pires, and G. Monterzino, "Design, build and flight of the DEMON demonstrator UAV," in *11th AIAA Aviation Technology, Integration, and Operations (ATIO) Conference*, Virginia Beach VA, 2011.
- [19] A. Savvaris, A. Buonanno, R. Jamil, and A. Tsourdos, "Design and development of the DEMON UAV fluidic flight control system," in *AIAA Infotech@Aerospace (I@A) Conference*, Boston Massachusetts, 2013.
- [20] K. Chen, Z. Shi, J. Zhu, H. Wang, and J. Fu, "Roll aerodynamic characteristics study of an unmanned aerial vehicle based on circulation control technology," *Proceedings of the Institution of Mechanical Engineers, Part G: Journal of Aerospace Engineering*, vol. 233, no. 3, pp. 871–882, 2019.
- [21] Z. Shi, J. Zhu, X. Dai et al., "Aerodynamic characteristics and flight testing of a UAV without control surfaces based on circulation control," *Journal of Aerospace Engineering*, vol. 32, no. 1, article 04018134, 2019.
- [22] C. M. Hsiun and C. K. Chen, "Aerodynamic characteristics of a two-dimensional airfoil with ground effect," *Journal of Aircraft*, vol. 33, no. 2, pp. 386–392, 1996.
- [23] M. R. Ahmed, T. Takasaki, and Y. Kohama, "Aerodynamics of a NACA4412 airfoil in ground effect," *AIAA Journal*, vol. 45, no. 1, pp. 37–47, 2007.
- [24] J. Zerihan and X. Zhang, "Aerodynamics of a single element wing in ground effect," *Journal of Aircraft*, vol. 37, no. 6, pp. 1058–1064, 2000.
- [25] S. Mahon and X. Zhang, "Computational analysis of pressure and wake characteristics of an airfoil in ground effect," *Journal of Fluids Engineering*, vol. 127, no. 2, pp. 290–298, 2005.
- [26] Q. Qu, W. Wang, P. Liu, and R. K. Agarwal, "Airfoil aerodynamics in ground effect for wide range of angles of attack," *AIAA Journal*, vol. 53, no. 4, pp. 1048–1061, 2015.
- [27] M. Nirooei, "Aerodynamic and static stability characteristics of airfoils in extreme ground effect," *Proceedings of the Institution of Mechanical Engineers, Part G: Journal of Aerospace Engineering*, vol. 232, no. 6, pp. 1134–1148, 2018.
- [28] P. J. Roache, "Perspective: a method for uniform reporting of grid refinement studies," *ASME Journal of Fluids Engineering*, vol. 116, no. 3, pp. 405–413, 1994.
- [29] M. G. Alexander, S. G. Anders, S. K. Johnson, J. P. Florance, and D. F. Keller, *Trailing Edge Blowing on a Two-Dimensional Six-Percent Thick Elliptical Circulation Control Airfoil up to Transonic Conditions*, NASA Langley Research Center, 2005.
- [30] Y. Li and N. Qin, "Airfoil gust load alleviation by circulation control," *Aerospace Science and Technology*, vol. 98, article 105622, 2020.
- [31] H. Y. Xu, C. L. Qiao, H. Q. Yang, and Z. Y. Ye, "Active circulation control on the blunt trailing edge wind turbine airfoil," *AIAA Journal*, vol. 56, no. 2, pp. 554–570, 2018.